Estimation of microfracture porosity in deep carbonate reservoirs based on 3D rock-physics templates

Mengqiang Pang[1], Jing Ba[1], Li-Yun Fu[2], José M. Carcione[3], Uti I. Markus[1], and Lin Zhang[1]

Abstract

Carbonate reservoirs in the S area of the Tarim Basin (China) are ultradeep hydrocarbon resources, with low porosity, complex fracture systems, and dissolved pores. Microfracturing is a key factor of reservoir connectivity and storage space. We have performed measurements on limestone samples, under different confining pressures, and we used the self-consistent approximation model and the Biot-Rayleigh theory of double porosity to study the microfractures. We have computed the fluid properties (mainly oil) as a function of temperature and pressure. Using the dependence of seismic Q on the microfractures, a multiscale 3D rock-physics template (RPT) is built, based on the attenuation, P-wave impedance, and phase velocity ratio. We estimate the ultrasonic and seismic attenuation with the spectral-ratio method and the improved frequency-shift method, respectively. Then, calibration of the RPTs is performed at ultrasonic and seismic frequencies. We use the RPTs to estimate the total and microfracture porosities. The results indicate that the total porosity is low and the microfracture porosity is relatively high, which is consistent with the well log data and actual oil production reports. This work presents a method for identification of deep carbonate reservoirs by using the microfracture porosity estimated from the 3D RPT, which could be exploited in oil and gas exploration.

Introduction

With the advancement of petroleum exploration techniques, developments have been extended to the field of deep and ultradeep oil-gas resources (Zou et al., 2014), such as carbonate reservoirs below 7 km depth in the S area of the Tarim Basin, Xinjiang, China. These reservoirs develop faults, dissolved pores, and complex fracture systems (Lan et al., 2015). Faults and microfractures develop under compression and are related to karst channels, where water infiltration results in a dissolved system (Zhang and Wang, 2004; Ni et al., 2017; Li et al., 2019b).

Seismic waves carry information about the subsurface characteristics. For interpretation purposes, an accurate rock-physics model is essential (Zhang et al., 2019a). Based on the Biot and Biot/squirt (BISQ) theories, Tang (2011) proposes a theoretical model of wave propagation in complex structures including the interaction between pores and microcracks. Ba et al. (2011) introduce the Biot-Rayleigh (BR) equations, which are based on the classic Biot theory and are appropriate to describe propagation in a double-porosity rock containing local fabric heterogeneities.

Rock-physics templates (RPTs) based on theoretical models can relate the seismic properties to the reservoir characteristics (Dvorkin and Mavko, 2006; Carcione and Avseth, 2015; Picotti et al., 2018). Classic 2D RPTs use the acoustic impedance and phase velocity ratio (the ratio of P- and S-wave velocities V_P/V_S) to establish a quantitative relationship between the wave response and lithology, porosity, and saturation (Odegaard and Avseth, 2004; Chi and Han, 2009; Ba et al., 2013a, 2013b; Hao et al., 2016). Gupta et al. (2012) establish an RPT by using the Kuster-Toksöz model to detect thin sandstone reservoirs in the Cambay Basin and obtained an isobath map of the oil layer. Ba et al. (2013a, 2013b) use the BR equations to build multiscale RPTs for detecting hydrocarbons in limestone reservoirs.

Experiments and theories show that microfractures are the dominant cause for wave dispersion and attenuation (Crampin and Bamford, 1977; Hudson, 1981; Chapman, 2003; Gurevich et al., 2009; Vernik and Kachanov, 2010; Carcione et al. 2013; Tillotson et al., 2014; Ba et al., 2017; Bouchaala et al., 2019; Cheng et al., 2019). Ali and Jakobsen (2011) detect microfractures from velocity and

[1]Hohai University, School of Earth Sciences and Engineering, Nanjing 211100, China. E-mail: pmq@hhu.edu.cn; baj08@petrochina.com.cn (corresponding author); marcusuti4u@gmail.com; zlin@hhu.edu.cn.

[2]China University of Petroleum (East China), Key Laboratory of Deep Oil and Gas, 66 Changjiang West Road, Huangdao District, Qingdao 266580, Shandong, China. E-mail: lfu@upc.edu.cn.

[3]Hohai University, School of Earth Sciences and Engineering, Nanjing 211100, China; and Istituto Nazionale di Oceanografia e di Geofisica Sperimentale (OGS), Borgo Grotta Gigante 42c, Sgonico, Trieste 34010, Italy. E-mail: jose.carcione@gmail.com.

Manuscript received by the Editor 2 December 2019; revised manuscript received 1 February 2020; published ahead of production 5 April 2020. This paper appears in *Interpretation*, Vol. 8, No. 4 (November 2020); p. 1–10, 14 FIGS.

http://dx.doi.org/10.1190/INT-2019-0258.1.

attenuation as a function of frequency and azimuth. Comparing experiment with theory, Guo et al. (2018) find that the microfracture density affects the scattering, dispersion, and attenuation of the P waves, especially at low frequencies. Cao et al. (2018) obtain the same conclusion by analyzing the geology and well-log data of carbonate reservoirs in the Tarim Basin. When the 2D RPTs are applied to deep carbonate reservoirs, the effects of complex pore structures (with microfractures) are likely to be incorrectly attributed to porosity or fluid type (Li et al., 2019a). Hence, the effect of microfractures on seismic waves becomes an important issue and has to be considered.

To characterize the effects of dissolved pores and microfractures in carbonates, we apply the self-consistent approximation (Berryman, 1980, SCA) and the BR equations to build RPTs, including temperature and pressure effects (Batzle and Wang, 1992). Then, the templates are calibrated based on ultrasonic experiments and seismic data, to predict the microfracture porosity.

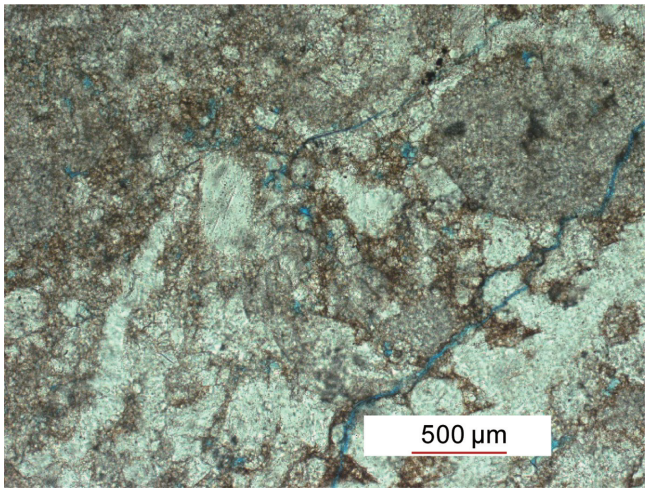

Figure 1. Thin section of a carbonate sample, collected at 7363 m in depth.

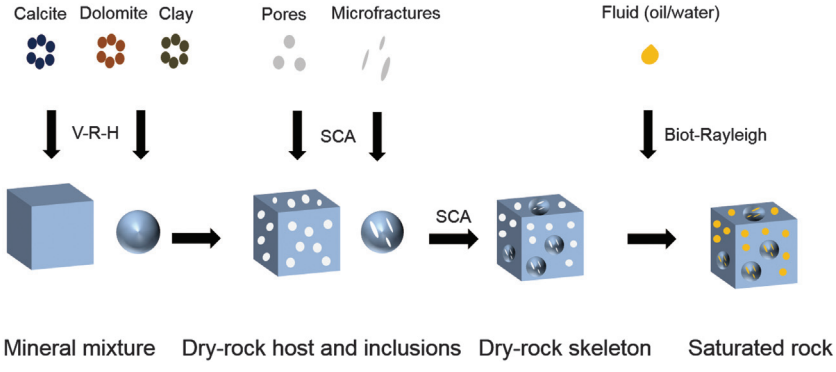

Figure 2. Flowchart of the rock-physics modeling.

3D RPTs

Rock-physics model of carbonate rocks

The area under study is located in the Shuntuoguole uplift, formed in the Caledonian-Hercynian orogeny, when multiphase faulting, fracturing, and fluid reformation occurred, resulting in a diversity of reservoir rocks (Ni et al., 2017). In this uplift, there is a complete source-reservoir-caprock assemblage in the Lower Paleozoic Formations, suggesting potential hydrocarbon accumulations. The main reservoir sections of the Ordovician carbonate rocks are the upper members from the Yijianfang to the Yingshan Formation (Wang et al., 2019). The reservoir thickness is approximately 110 m, and the lithology is mainly limestone.

The in situ reservoirs are characterized by their high temperature (>150°C) and confining pressure (>160 MPa). The caves, dissolved pores, microfractures, and vugs are formed by multistage strike-slip faulting as well as dissolution and alteration. Figure 1 displays a thin section of the limestone sample, showing dissolved pores in the matrix and several microfractures with different apertures. The surface porosities are extremely low (<1%). In Figure 1, the mineral percentage of rock sample is calcite 97% and dolomite 3%.

Figure 2 shows the modeling procedure. First, the mineral composition of the rocks is analyzed. The target reservoir rocks are mainly limestones with high-calcite content and a small amount of dolomite and clay. The bulk and shear moduli of calcite, dolomite, and clay are 63.7 and 31.7 GPa, 76.4 and 49.7 GPa, 25 and 9 GPa, respectively. The Voigt-Reuss-Hill (Voigt, 1910; Reuss, 1929; Hill, 1952, VRH) equation is used to estimate the elastic moduli of the mineral mixture.

The dissolved pores and microfractures are considered stiff and soft, which are of spherical and oblate shapes, whose aspect ratios are assumed to be 1 and 0.0003, respectively. The microfracture porosity is $\phi_C = \phi_{20} \bullet v_2$, where $\phi_{20} = 0.012$ and v_2 are the porosity and the volume content of the inclusions, respectively. The dry-rock moduli are obtained by mixing the host matrix and inclusions, based on the SCA equation (Berryman, 1980),

$$\sum x_i (K_i - K^*_{\mathrm{SC}}) P^{*i} = 0, \tag{1a}$$

$$\sum x_i (\mu_i - \mu^*_{\mathrm{SC}}) Q^{*i} = 0, \tag{1b}$$

where K^*_{SC} and μ^*_{SC} are the bulk and shear moduli of the dry rock, respectively, i indicates the mineral phase or pore space with a corresponding volume fraction x_i and bulk and shear moduli K_i and μ_i, and P^{*i} and Q^{*i} are the corresponding geometry factors of the ith component.

The bulk modulus and density of the fluid are estimated by using the equation

proposed by Batzle and Wang (1992), at the in-situ condition (temperature: 180°C and pore pressure: 80 MPa). The BR theory is used for fluid substitution (Ba et al., 2011), whose differential equations of motion are

$$N\nabla^2\mathbf{u}+(A+N)\nabla\varepsilon+Q_1\nabla(\zeta^{(1)}+\phi_C\varsigma)+Q_2\nabla(\zeta^{(2)}-\phi_1\varsigma)$$
$$=\rho_{11}\ddot{\mathbf{u}}+\rho_{12}\ddot{\mathbf{U}}^{(1)}+\rho_{13}\ddot{\mathbf{U}}^{(2)}+b_1(\dot{\mathbf{u}}-\dot{\mathbf{U}}^{(1)})+b_2(\dot{\mathbf{u}}-\dot{\mathbf{U}}^{(2)}) \quad (2a)$$

$$Q_1\nabla\varepsilon+R_1\nabla(\zeta^{(1)}+\phi_C\varsigma)=\rho_{12}\ddot{\mathbf{u}}+\rho_{22}\ddot{\mathbf{U}}^{(1)}-b_1(\dot{\mathbf{u}}-\dot{\mathbf{U}}^{(1)}) \quad (2b)$$

$$Q_2\nabla\varepsilon+R_2\nabla(\zeta^{(2)}-\phi_1\varsigma)=\rho_{13}\ddot{\mathbf{u}}+\rho_{33}\ddot{\mathbf{U}}^{(2)}-b_2(\dot{\mathbf{u}}-\dot{\mathbf{U}}^{(2)}) \quad (2c)$$

$$\phi_C(Q_1\varepsilon+R_1(\zeta^{(1)}+\phi_C\varsigma))-\phi_1(Q_2\varepsilon+R_2(\zeta^{(2)}-\phi_1\varsigma))$$
$$=\frac{1}{3}\rho_f\ddot{\varsigma}R_0^2\frac{\phi_1^2\phi_C\phi_{20}}{\phi_{10}}+\frac{1}{3}\frac{\eta\phi_1^2\phi_C\phi_{20}}{\kappa_1}\cdot\varsigma R_0^2, \quad (2d)$$

where $\mathbf{u}$, $\mathbf{U}^{(1)}$, and $\mathbf{U}^{(2)}$ are the average particle displacements of the solid skeleton, fluid phase 1 (the fluid in the host), and fluid phase 2 (the fluid in the inclusions containing microfractures), respectively, whereas ε, $\zeta^{(1)}$, and $\zeta^{(2)}$ are the corresponding displacement divergence fields of the three phases. The scalar ς represents the fluid variation in the local fluid flow; ϕ_{10} and ϕ_1 are the porosities of the host medium and the stiff pore phase, respectively; κ_1 is the permeability of the host medium; η and ρ_f are the fluid viscosity and density of the host, respectively; A, N, Q_1, Q_2, R_1, and R_2 are stiffnesses; ρ_{11}, ρ_{12}, ρ_{13}, ρ_{22}, and ρ_{33} are density coefficients; R_0 is the inclusion radius; and b_1 and b_2 are Biot's dissipation coefficients.

By substituting a plane P-wave kernel into equation 2a–2d to compute the complex wave number k, the phase velocity and quality factor are (Carcione, 2014)

$$V_P=[\mathrm{Re}(v^{-1})]^{-1}, \quad (3a)$$

$$Q=\frac{\mathrm{Re}(v^2)}{\mathrm{Im}(v^2)}, \quad (3b)$$

where $v=\omega/k$ is the complex velocity.

Wave responses and microfracture porosity

The porosity is 3%; the proportion of calcite, dolomite, and clay is 91.3%, 5.2%, and 3.5%, respectively; the inclusion radius is 50 μm; the porosity of the inclusions is 0.012; and the aspect ratio of the microfractures is 0.0003. The properties of oil and water are as follows: the bulk moduli = 0.79 and 2.23 GPa, the densities = 0.698 and 0.927 g/cm^3, and the viscosities = 0.002289 and 0.00065 Pa s. The properties of the mineral mixture and rock skeleton are computed with the VRH average and SCA equations, respectively. Assuming full oil saturation, the effects of the microfracture porosity on the P-wave attributes are analyzed by assuming different microfracture porosities. Figure 3 shows the P-wave velocity dispersion and attenuation as a function of frequency. The dispersion and attenuation increase with the microfracture porosity, with a slight shift of the relaxation peaks to the high frequencies. Figure 4 shows the same properties as a function of the microfracture porosity and different total porosities. The velocity gradually decreases and the attenuation increases with increasing microfracture porosity and total porosity. Figure 5 shows that the S-wave velocity decreases and the phase velocity ratio increases with increasing microfracture porosity, with the trend being the same at different total porosities.

Multiscale 3D RPTs of carbonate rocks

Three-dimensional RPTs are built by using the dependence of the seismic properties on total porosity

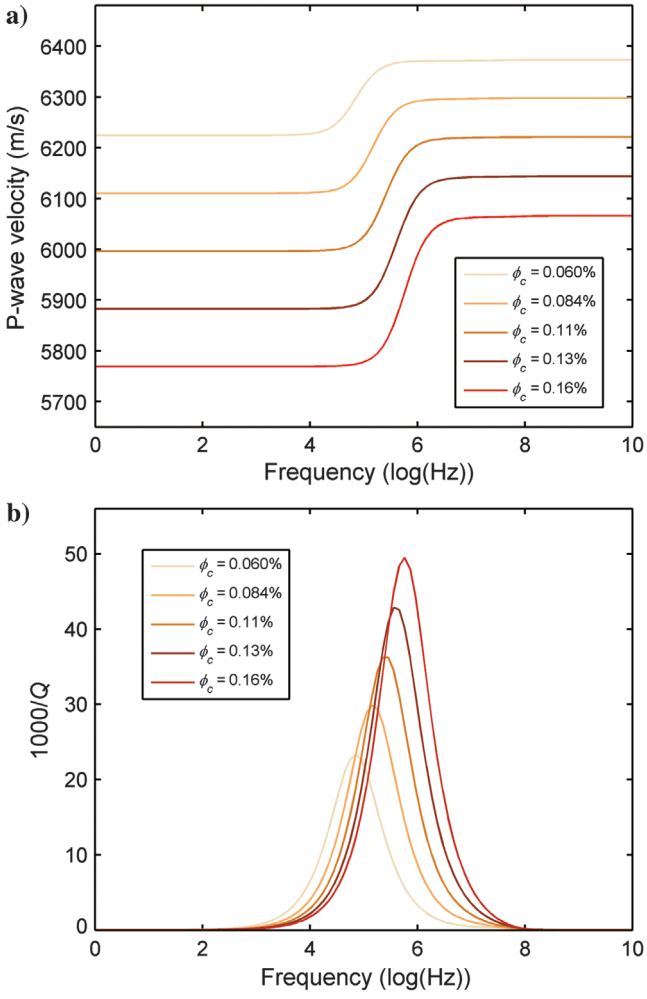

Figure 3. Effects of microfracture porosity on (a) P-wave velocity dispersion and (b) attenuation as a function of frequency.

and microfracture porosity. At 1 MHz, the inclusion radius is assumed to be 50 μm, and we consider full water and oil saturations. The 3D templates are given in Figure 6, where the results show that the P-wave attenuation is sensitive to microfracture porosity. The attenuation and V_P/V_S increase with increasing total porosity and microfracture porosity, whereas the impedance (Ip) decreases. The sensitivity is similar for water and oil, and the difference increases when the two types of porosity increase.

If we consider an inclusion radius of 50 mm, attenuation has a peak at seismic frequencies. Figure 7 shows the 3D RPTs at 35 Hz. This template is used to estimate the total porosity and microfracture porosity from seismic data.

Multiscale calibrations of the RPTs

Ultrasonic laboratory experiment and attenuation analysis

The microfractures tend to close gradually with increasing confining pressure (Wei et al., 2019; Pang et al.,

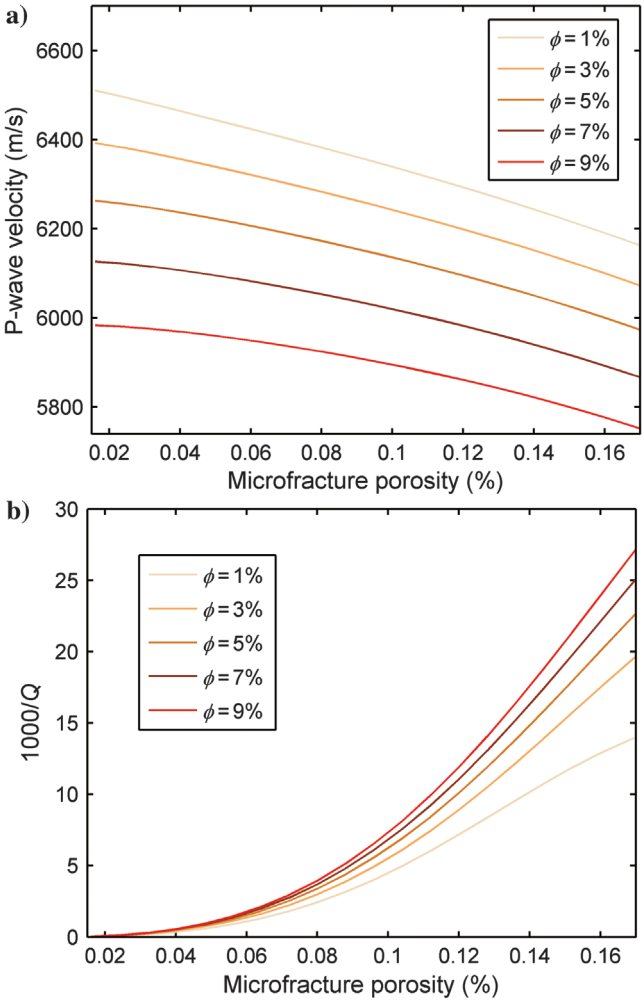

Figure 4. (a) P-wave velocity and (b) attenuation as a function of the microfracture porosity at 1 MHz. Results at different total porosities are given.

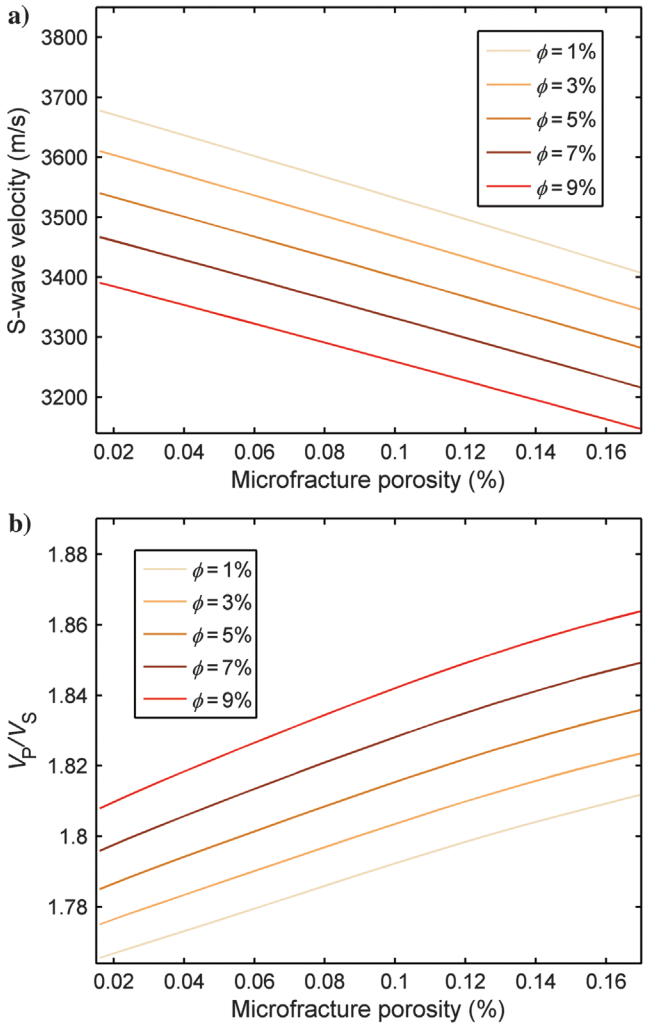

Figure 5. (a) S-wave velocity and (b) phase velocity ratio as a function of microfracture porosity. Results at different total porosities are given.

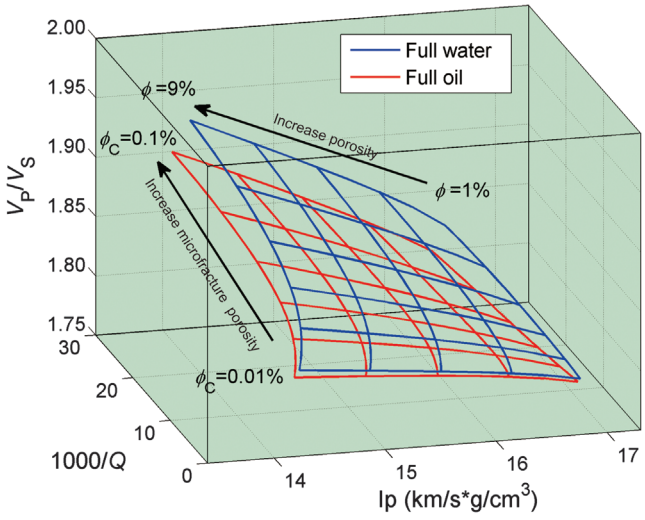

Figure 6. Three-dimensional RPTs at 1 MHz.

2019b). To investigate the effects of the microfractures, ultrasonic experiments at 1 MHz are performed at different confining pressures for two limestone samples. The porosity of samples A and B (collected from the Ordovician Formations of the basin) is 2.5% and 0.71%, respectively, the permeabilities are 0.023 and 1.559 mD, and the measured dry-rock densities are 2.66 and 2.67 g/cm^3, respectively. The experiments were performed at a pore pressure of 10 MPa and a temperature of 140°C. The experimental setup of Guo et al. (2009) is used to obtain the wave velocity.

The samples are first fully saturated with oil and then jacketed and put in a sealed vessel, and kerosene (oil) is injected into the samples up to a given pore pressure. The waveforms are recorded at confining pressures of 20, 25, 30, 35, 40, 45, 50, 60, and 70 MPa, and the velocities are obtained by picking the first arrivals of the waveforms. On the basis of the confining pressure, pore pressure, and P- and S-wave velocities of the samples, the microfracture porosity ϕ_C is estimated by using an inversion method (see equation A-1 in Appendix A). The quality factor Q is determined with the spectral-ratio method by using a reference standard material with a very high quality factor (see equation A-2 in Appendix A).

Figure 8a shows the microfracture porosity, which decreases as the confining pressure increases. The P- and S-wave velocities show the same trend (Figure 8b). Figure 9 shows that the attenuation of the P wave increases with the microfracture porosity. The attenuation of sample B is higher than that of sample A at the same microfracture porosity.

Calibration of the RPT at ultrasonic frequencies

Before the RPTs are applied, it is necessary to calibrate the templates. Figure 10 shows the ultrasonic data of the two samples (scatters), compared with the RPT after calibration at 1 MHz, where the black curves indicate isolines of total porosity and the red curves indicate isolines of microfracture porosity. The color bar of the scatters indicates microfracture porosity, which

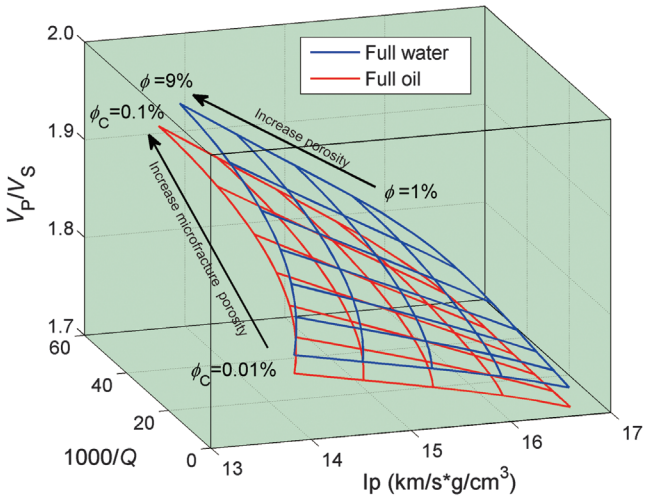

Figure 7. Three-dimensional RPTs at 35 Hz.

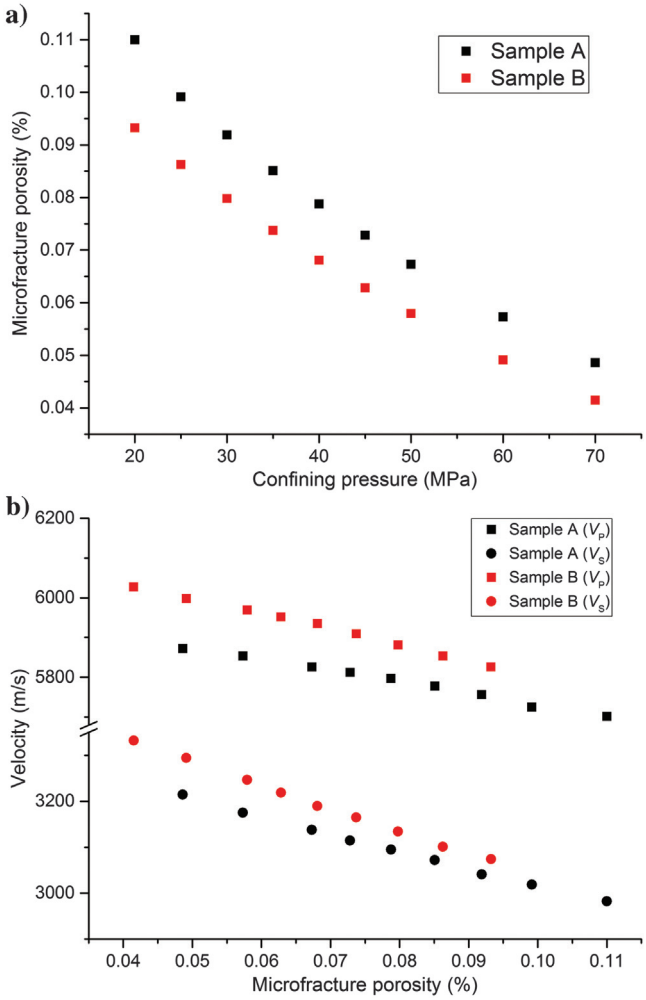

Figure 8. (a) Microfracture porosity as a function of confining pressure. (b) P- and S-wave velocities as a function of microfracture porosity.

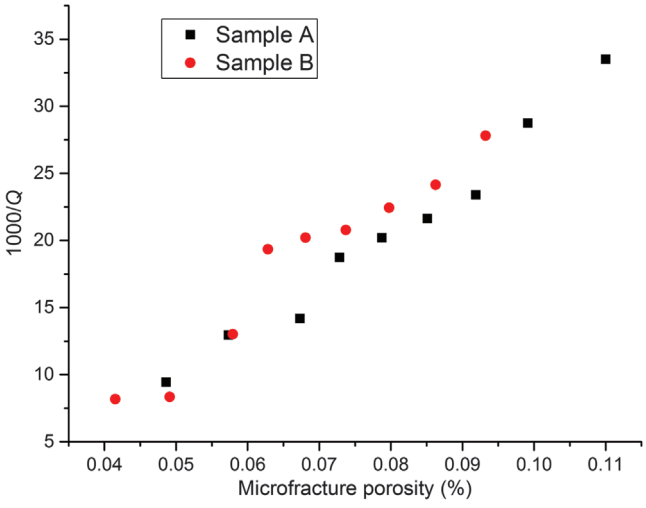

Figure 9. P-wave attenuation as a function of microfracture porosity.

agree well with the red curves. The same trend can be observed between the data and template for the relations between attenuation, impedance and V_P/V_S and microfracture porosity.

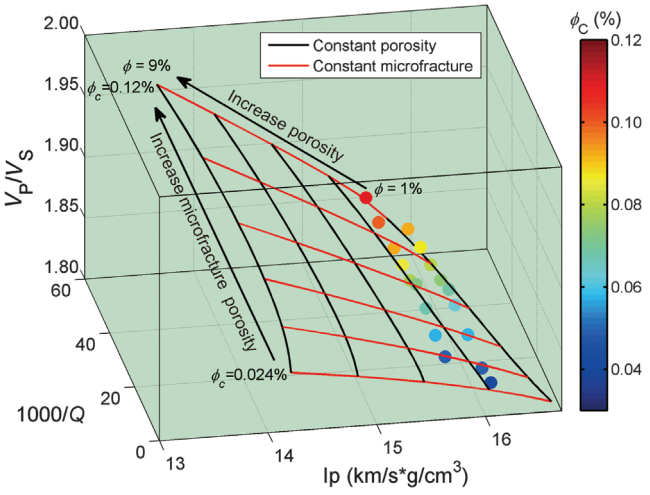

Figure 10. Three-dimensional RPT at 1 MHz and experimental data.

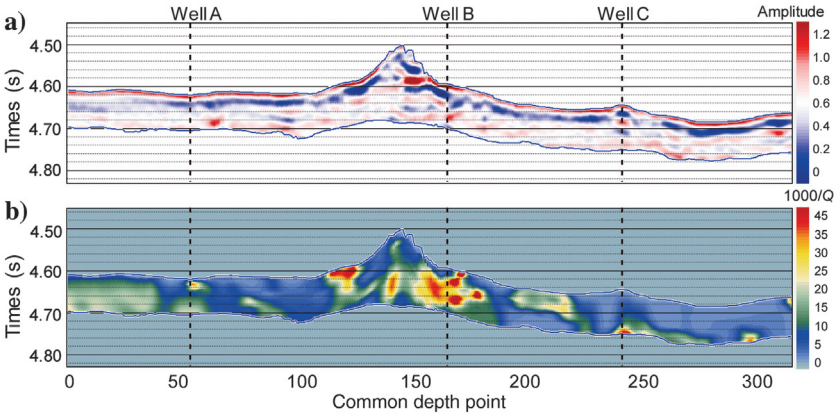

Figure 11. (a) Seismic amplitude and (b) attenuation profiles.

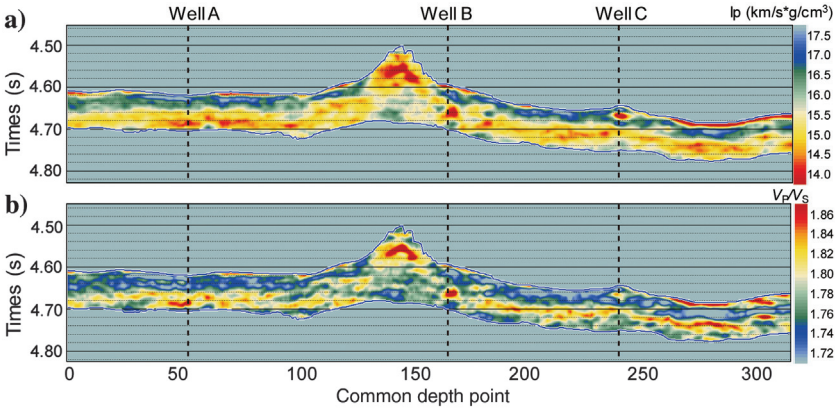

Figure 12. Two-dimensional seismic lines of (a) P-wave impedance and (b) V_P/V_S of the formation.

Estimation of attenuation of the reservoirs

Recently, seismic attenuation has been used to evaluate unconventional fractured reservoirs (Li et al., 2015a, 2015b, 2016). The improved frequency-shift method is used to estimate the attenuation of the seismic data (equation A-3 in Appendix A). Figure 11 shows a 2D seismic line, where the dotted lines indicate the positions of three oil wells. Figure 11a and 11b shows the seismic amplitude and attenuation of the target Yijianfang Formation, respectively, where the red zone indicates strong attenuation and the blue zone indicates weak attenuation (Figure 11b). The results show that there are attenuation anomalies in the three oil wells.

Calibration of RPT at seismic frequency

Due to the complex pore structures, the P-wave velocities at different frequencies for the same rock are different, which is reflected in the wave dispersion on multiscale data. The P-wave attenuation varies with frequency correspondingly. By using the BR equation, the P-wave velocity and dispersion at each frequency of multiscale waveform data can be modeled (Ba et al., 2013b). The ultrasonic band focuses on the microscopic scale, whereas the seismic dissipation is associated with mesoscopic-scale heterogeneity (Ba et al., 2008). By applying the method from ultrasonic band to seismic band, the angular frequency in the theoretical equations changes correspondingly. However, the mesoscopic heterogeneity (which dominates wave responses in the seismic band) is considered instead of microscopic heterogeneity; that is, the inclusion radius and microfractures' aspect ratio are considered to calibrate the seismic data. The effects of the pore structure can be analyzed by building an RPT at the seismic band. By using the actual field data in the comparison with the RPT in seismic frequency band, the availability of the method can be verified.

The RPT is calibrated at 35 Hz. The phase velocity ratio and the P-wave impedance are obtained by 3D pre-stack inversion (shown in Figure 12), and together with attenuation, we extract the above quantities at the borehole location (well B) and from the Yijianfang Formation to calibrate the template. Figure 13 shows a comparison between the seismic data (scatters) and the corresponding template. The color bar indicates the log interpretation porosity, which is in agreement with the template. According to the seismic scatters, the porosity is generally low, consistent with the geologic characteristics of the target formation. Rocks with relatively high porosity (>3%) may be considered for potential oil

production. Because the P-wave impedance, attenuation and V_P/V_S can be obtained from seismic data, a quantitative prediction of reservoir microfracture porosity can be achieved by overlaying the data points on the template.

Prediction of reservoir porosity and microfracture porosity

A quantitative prediction of reservoir porosity and microfracture porosity is performed for the Yijianfang Formation in the 2D survey line crossing wells A, B, and C. The P-wave impedance, attenuation, and V_P/V_S are overlapped onto the RPT, and the porosities are estimated accordingly.

Figure 14a shows the 2D profile of reservoir porosity, where the results indicate values less than 10%, and they also indicate that, mostly, the target formation rocks are tight layers with extremely low porosity. Some areas of relatively high porosity can be observed at wells A, B, and C. The porosity obtained from well log B is compared to the seismic profile, showing good agreement.

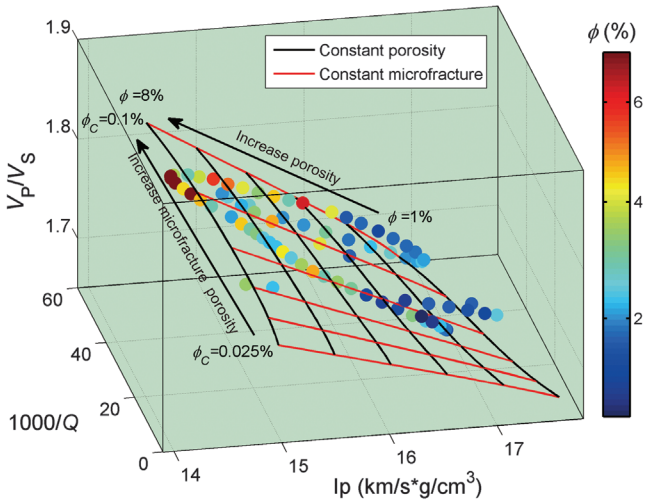

Figure 13. Three-dimensional RPT at 35 Hz and the field data.

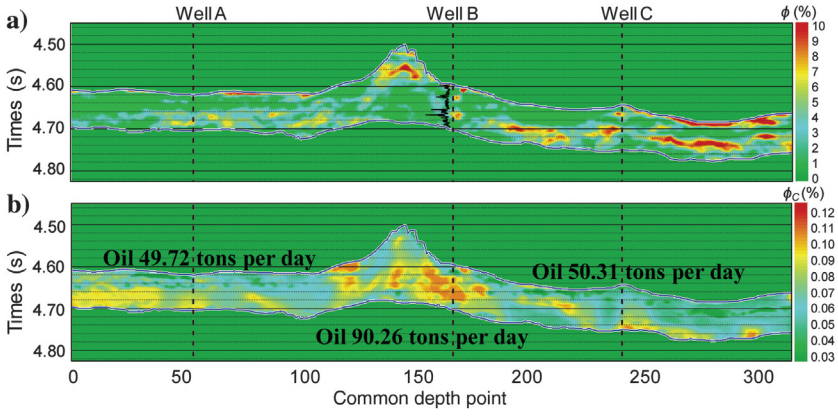

Figure 14. (a) Total porosity and (b) microfracture porosity of the reservoirs. The log porosity of well B is shown.

Figure 14b shows that the microfracture porosity is high, in agreement with the actual geologic characteristics of the carbonate formation. The development of reservoir microfractures at the borehole location of wells A and C is less pronounced with well B showing a better connectivity and storage capacity. The oil production report of well B indicates 90.26 tons per day, whereas wells A and C yield 49.72 and 50.31 tons per day, respectively. The results agree with the actual production of the three wells. The total porosity and microfracture porosity effectively serve to identify high-quality reservoirs.

Conclusions

The rock-physics characteristics of deep carbonate reservoirs are analyzed based on the SCA and BR theory, which constitute a rock-physics model including microfractures. Then, the wave attenuation, impedance, and phase-velocity ratio are used to build multiscale 3D RPTs. Ultrasonic experiments are performed on limestone samples, and the spectral-ratio method is used to estimate the P-wave attenuation, showing that this is sensitive to the microfracture porosity. On the other hand, the seismic properties are estimated by using the improved frequency-shift method and pre-stack inversion. The laboratory and seismic data are then used to calibrate the RPTs, which are applied to the prediction of hydrocarbon saturation in deep carbonate reservoirs.

The results show that the total porosity is generally low but the microfracture porosity is relatively high, which is consistent with the actual geologic features of ultradeep carbonate reservoirs in the target formation. The porosity prediction based on seismic data at the location of well B is consistent with the log profile, and the microfracture inversion results effectively reflect the oil production state of the wells. The study shows that besides total porosity, microfracture porosity is a critical factor for identifying high-quality reservoirs in deep carbonate formations. Different from the traditional prediction methods, the 3D RPTs in this paper make use of phase velocities and P-wave attenuation simultaneously for 3D intersection analysis of multiscale data. Because three attributes can be adopted to establish the template based on multiscale wave data, it is helpful in solving the interpretation problems for deep reservoirs with complex microstructures, where the issue of multisolution exists in geophysical inversion.

Acknowledgments

The authors are grateful to the Jiangsu Innovation and Entrepreneurship Plan, the Specially Appointed Professor Plan of Jiangsu Province, and the National Natural Science Foundation of China (grant no. 41974123).

Data and materials availability

Data associated with this research are available and can be obtained by contacting the corresponding author.

Appendix A

The microfracture porosity inversion method is (David and Zimmerman, 2012; Zhang et al., 2019b)

$$\phi_c(p) = \frac{4\pi\alpha_p}{3}\Gamma_p, \tag{A-1}$$

where p is the effective pressure, Γ_p is the microfracture density, and α_p is the aspect ratio of the microfractures.

The spectral-ratio method is (Toksöz et al., 1979; Ba et al., 2019)

$$\ln\left[\frac{A_1(f)}{A_2(f)}\right] = -\frac{\pi x}{QV}f + \ln\left[\frac{G_1(x)}{G_2(x)}\right], \tag{A-2}$$

where f is the frequency, $A_1(f)$ and $A_2(f)$ are the amplitude spectra of the rock sample and standard material, respectively, x is the wave propagation distance, V is the wave velocity, and $G_1(x)/G_2(x)$ is the sample/standard geometric factor.

The improved frequency-shift method is (Pang et al., 2019a, 2019b)

$$Q = \frac{\sqrt{\pi^5}tf_{C1}f_{C0}^2}{16(f_{C0}^2 - f_{C1}^2)}, \tag{A-3}$$

where t is the propagation time, and f_{C0} and f_{C1} are the centroid frequencies of the signal before and after propagation, respectively.

References

Ali, A., and M. Jakobsen, 2011, Seismic characterization of reservoirs with multiple fracture sets using velocity and attenuation anisotropy data: Journal of Applied Geophysics, **75**, 590–602, doi: 10.1016/j.jappgeo.2011.09.003.

Ba, J., H. Cao, J. M. Carcione, G. Tang, X. Yan, W. Sun, and J. Nie, 2013a, Multiscale rock-physics templates for gas detection in carbonate reservoirs: Journal of Applied Geophysics, **93**, 77–82, doi: 10.1016/j.jappgeo.2013.03.011.

Ba, J., J. M. Carcione, and J. Nie, 2011, Biot-Rayleigh theory of wave propagation in double-porosity media: Journal of Geophysical Research, **116**, B06202, doi: 10.1029/2010JB008185.

Ba, J., R. Ma, J. M. Carcione, and S. Picotti, 2019, Ultrasonic wave attenuation dependence on saturation in tight oil siltstones: Journal of Petroleum Science and Engineering, **179**, 1114–1122, doi: 10.1016/j.petrol.2019.04.099.

Ba, J, J. Nie, H. Cao, and H. Yang, 2008, Mesoscopic fluid flow simulation in double-porosity rocks. Geophysical Research Letters, **35**, L04303.

Ba, J., W. Xu, L. Fu, J. M. Carcione, and L. Zhang, 2017, Rock anelasticity due to patchy-saturation and fabric heterogeneity: A double-double porosity model of wave propagation: Journal of Geophysical Research: Solid Earth, **122**, 1949–1976, doi: 10.1002/2016JB013882.

Ba, J., X. Yan, Z. Chen, G. Xu, C. Bian, H. Cao, F. Yao, and W. Sun, 2013b, Rock physics model and gas saturation inversion for heterogeneous gas reservoirs: Chinese Journal of Geophysics (in Chinese), **56**, 1696–1706, doi: 10.6038/cjg20130527.

Batzle, M. L., and Z. Wang, 1992, Seismic properties of pore fluids: Geophysics, **57**, 1396–1408, doi: 10.1190/1.1443207.

Berryman, J. G., 1980, Long-wavelength propagation in composite elastic media: Journal of Acoustical Society of America, **68**, 1809–1831, doi: 10.1121/1.385171.

Bouchaala, F., M. Y. Ali, J. Matsushima, Y. Bouzidi, E. T. Takougang, A. A. Mohamed, and A. A. Sultan, 2019, Scattering and intrinsic attenuation as a potential tool for studying of a fractured reservoir: Journal of Petroleum Science and Engineering, **174**, 533–543, doi: 10.1016/j.petrol.2018.11.058.

Cao, Z., X. Li, J. Liu, X. Qin, S. Sun, and Z. Li, 2018, Carbonate fractured gas reservoir prediction based on P-wave azimuthal anisotropy and dispersion: Journal of Geophysics and Engineering, **15**, 2139–2149. doi: 10.1088/1742-2140/aabe58.

Carcione, J. M., 2014, Wavefields in real media. Theory and numerical simulation of wave propagation in anisotropic, anelastic, porous and electromagnetic media, 3rd ed.: Elsevier.

Carcione, J. M., and P. Avseth, 2015, Rock-physics templates for clay-rich source rocks: Geophysics, **80**, no. 5, D481–D500, doi: 10.1190/GEO2014-0510.1.

Carcione, J. M., B. Gurevich, J. E. Santos, and S. Picotti, 2013, Angular and frequency dependent wave velocity and attenuation in fractured porous media: Pure and Applied Geophysics, **170**, 1673–1683, doi: 10.1007/s00024-012-0636-8.

Chapman, M., 2003, Frequency-dependent anisotropy due to meso-scale fractures in the presence of equant porosity: Geophysical Prospecting, **51**, 369–379, doi: 10.1046/j.1365-2478.2003.00384.x.

Cheng, W., J. Ba, L. Fu, and M. Lebedev, 2019, Wave-velocity dispersion and rock microstructure: Journal of Petroleum Science and Engineering, **183**, 106466, doi: 10.1016/j.petrol.2019.106466.

Chi, X., and D. Han, 2009, Lithology and fluid differentiation using a rock physics template: The Leading Edge, **28**, 60–65, doi: 10.1190/1.3064147.

Crampin, S., and D. Bamford, 1977, Inversion of P-wave velocity anisotropy: Geophysical Journal International, **49**, 123–132, doi: 10.1111/j.1365-246X.1977.tb03704.x.

David, E. C., and R. W. Zimmerman, 2012, Pore structure model for elastic wave velocities in fluid-saturated sandstones: Journal of Geophysical Research: Solid Earth, **117**, B07210, doi: 10.1029/2012JB009195.

Dvorkin, J., and G. Mavko, 2006, Modeling attenuation in reservoir and nonreservoir rock: The Leading Edge, **25**, 194–197, doi: 10.1190/1.2172312.

Guo, J., D. Shuai, J. Wei, P. Ding, and B. Gurevich, 2018, P-wave dispersion and attenuation due to scattering by aligned fluid saturated fractures with finite thickness: Theory and experiment: Geophysical Journal International, **215**, 2114–2133, doi: 10.1093/gji/ggy406.

Guo, M., L. Fu, and J. Ba, 2009, Comparison of stress-associated coda attenuation and intrinsic attenuation from ultrasonic measurements: Geophysical Journal International, **178**, 447–456, doi: 10.1111/j.1365-246X.2009.04159.x.

Gupta, S. D., R. Chatterjee, and M. Y. Farooqui, 2012, Rock physics template (RPT) analysis of well logs and seismic data for lithology and fluid classification in Cambay Basin: International Journal of Earth Sciences, **101**, 1407–1426, doi: 10.1007/s00531-011-0736-1.

Gurevich, B., M. Brajanovski, R. J. Galvin, T. M. Muller, and J. Toms-Stewart, 2009, P-wave dispersion and attenuation in fractured and porous reservoirs-poroelasticity approach: Geophysical Prospecting, **57**, 225–237, doi: 10.1111/j.1365-2478.2009.00785.x.

Hao, Z., J. Ba, L. Zhang, Q. Zeng, R. Jiang, J. Liu, W. Qian, W. Tan, and W. Cheng, 2016, Rock physics inversion workflow on reservoir parameters: A case study of seismic hydrocarbon detection in large-area tight dolomite reservoirs: Journal of Seismic Exploration, **25**, 561–588.

Hill, R., 1952, The elastic behaviour of a crystalline aggregate: Proceedings of the Physical Society, **65**, 349–354, doi: 10.1088/0370-1298/65/5/307.

Hudson, J. A., 1981, Wave speeds and attenuation of elastic waves in material containing cracks: Geophysical Journal International, **64**, 133–150, doi: 10.1111/j.1365-246X.1981.tb02662.x.

Lan, X., X. Lu, Y. Zhu, and H. Yu, 2015, The geometry and origin of strike-slip faults cutting the Tazhong low rise megaanticline (central uplift, Tarim Basin, China) and their control on hydrocarbon distribution in carbonate reservoirs: Journal of Natural Gas Science and Engineering, **22**, 633–645, doi: 10.1016/j.jngse.2014.12.030.

Li, F., T. Zhao, T. Lin, and K. J. Marfurt, 2015b, Fracture characterization based on attenuation estimation from seismic reflection data using well-log-based localized spectral correction: URTeC, 1156–1166.

Li, F., H. Zhou, N. Jiang, J. Bi, and K. J. Marfurt, 2015a, Q estimation from reflection seismic data for hydrocarbon detection using a modified frequency shift method, Journal of Geophysics and Engineering, **12**, 577–586, doi: 10.1088/1742-2132/12/4/577.

Li, F., H. Zhou, T. Zhao, and K. J. Marfurt, 2016, Unconventional reservoir characterization based on spectrally corrected seismic attenuation estimation: Journal of Seismic Exploration, **25**, 447–461.

Li, H., Z. JiaJia, S. Cai, and H. Pan, 2019a, 3D rock physics template for reservoirs with complex pore structure (in Chinese): Chinese Journal of Geophysics, **62**, 2711–2723, doi: 10.6038/cjg2019K0672.

Li, Y., J. Sun, H. Wei, and S. Song, 2019b, Architectural features of fault-controlled karst reservoirs in the Tahe oilfield: Journal of Petroleum Science and Engineering, **181**, 106208, doi: 10.1016/j.petrol.2019.106208.

Ni, Z., T. Wang, M. Li, Z. Chen, G. Ou, and Z. Cao, 2017, Natural gas characteristics, fluid evolution, and gas charging time of the Ordovician reservoirs in the Shuntuoguole region, Tarim Basin, NW China: Geological Journal, **53**, 947–959. doi:10.1002/gj.2936.

Odegaard, E., and P. A. Avseth, 2004, Well log and seismic data analysis using rock physics templates: First Break, **22**, 37–43, doi: 10.3997/1365-2397.2004017.

Pang, M., J. Ba, J. M. Carcione, S. Picotti, J. Zhou, and R. Jiang, 2019a, Estimation of porosity and fluid saturation in carbonates from rock-physics templates based on seismic Q: Geophysics, **84**, no. 6, M25–M36, doi: 10.1190/geo2019-0031.1.

Pang, M., J. Ba, J. M. Carcione, A. Vesnaver, R. Ma, and T. Chen, 2019b, Analysis of attenuation rock-physics template of tight sandstones: Reservoir microcrack prediction (in Chinese): Chinese Journal of Geophysics, in press.

Picotti, S., J. M. Carcione, and J. Ba, 2018, Rock-physics templates for seismic *Q*: Geophysics, **84**, no. 1, MR13–MR23, doi: 10.1190/GEO2018-0017.1.

Reuss, A., 1929, Calculation of the flow limits of mixed crystals on the basis of the plasticity of monocrystals: Zeitschrift für Angewandte Mathematik und Mechanik, **9**, 49–58.

Tang, X., 2011, A unified theory for elastic wave propagation through porous media containing cracks—An extension of Biot's poroelastic wave theory (in Chinese): Science China Earth Sciences, **41**, 784–795.

Tillotson, P., M. Chapman, J. Sothcott, B. L. Augus, and X. Li, 2014, Pore fluid viscosity effects on P- and S-wave anisotropy in synthetic silica-cemented sandstone with aligned fractures: Geophysical Prospecting, **62**, 1238–1252, doi: 10.1111/1365-2478.12194.

Toksöz, M. N., H. D. Johnston, and A. Timur, 1979, Attenuation of seismic waves in dry and saturated rocks: I. Laboratory measurements: Geophysics, **44**, 681–690, doi: 10.1190/1.1440969.

Vernik, L., and M. Kachanov, 2010, Modeling elastic properties of siliciclastic rocks: Geophysics, **75**, no. 6, E171–E182, doi: 10.1190/1.3494031.

Voigt, W., 1910, Lehrbuch der Kirstallphysik: Teubner.

Wang, Q., H. Huang, H. Chen, and Y. Zhao, 2019, Secondary alteration of ancient Shuntuoguole oil reservoirs, Tarim Basin, NW China: Marine and Petroleum Geology, **111**, 202–218, doi:10.1016/j.marpetgeo.2019.08.013.

Wei, Y., J. Ba, L. Fu, R. Ma, L. Zhang, J. M. Carcione, and M. Guo, 2019, A study on effect of stress change on pore structure and elastic wave responses in tight sandstones (in Chinese): Chinese Journal of Geophysics, doi: 10.6038/cjg2019N0004.

Zhang, B., D. Yang, Y. Cheng, and Y. Zhang, 2019a, A unified poroviscoelastic model with esoscopic and microscopic heterogeneities: Science Bulletin, **64**, 1246–1254, doi: 10.1016/j.scib.2019.05.027.

Zhang, K., and D. Wang, 2004, Types of Karst-fractured and porous reservoirs in China's carbonates and the nature of the Tahe Oilfield in the Tarim Basin: Acta Geologica Sinica, **78**, 866–872, doi: 10.1111/j.1755-6724.2004.tb00208.x.

Zhang, L., J. Ba, L. Fu, J. M. Carcione, and C. Cao, 2019b, Estimation of pore microstructure by using the static and dynamic moduli: International Journal of Rock Mechanics and Mining Sciences, **113**, 24–30, doi: 10.1016/j.ijrmms.2018.11.005.

Zou, C., L. Hou, S. Hu, R. Zhu, S. Liu, Z. Yang, Z. Gu, Y. Fan, and C. Yang, 2014, Prospect of ultra-deep petroleum onshore China: Energy Exploration and Exploitation, **32**, 19–40, doi: 10.1260/0144-5987.32.1.19.

Biographies and photographs of authors are not available.